## PAPER

Check for updates

# A novel and sustainable synthesis-functionalization strategy for the oxidative cyclization towards 2,5-disubstituted-1,3,4-oxadiazoles using bentonite-supported copper(I) iodide as a green catalyst

Vinh Quang Tran,[ab] Dat Minh Tran,[ab] Minh Hai Tran,[ab] Phuong Hoang Tran [ab] and Hai Truong Nguyen [*ab]

This study developed a novel, sustainable approach for synthesizing 2,5-disubstituted-1,3,4-oxadiazoles *via* oxidative cyclization of hydrazones using a heterogeneous bentonite-supported copper(I) iodide (CuI/Bent-NH$_2$) as a catalyst. CuI/Bent-NH$_2$ was prepared through a two-step process: functionalization of natural bentonite clay with (3-aminopropyl)triethoxysilane (APTES) and subsequent immobilization of CuI. The structure of CuI/Bent-NH$_2$ was determined by methods such as FT-IR spectroscopy, Raman spectroscopy, XRD analysis, scanning electron microscopy (SEM), energy-dispersive X-ray spectroscopy (EDX), thermogravimetric analysis (TGA) and X-ray photoelectron spectroscopy (XPS), which confirmed successful surface modification, metal incorporation, and desirable structural and thermal properties of the material. The catalytic system efficiently promoted the oxidative cyclization of hydrazone derivatives in the presence of potassium persulfate as a green oxidant, and potassium carbonate as a base agent under optimized conditions (100 °C, DMSO, 5 h). A broad range of hydrazones bearing both electron-donating and electron-withdrawing substituents were converted into their corresponding oxadiazole products in moderate to good yields (up to 67%). Mechanistic studies proposed a radical-mediated pathway facilitated by Cu(II)/Cu(I) redox cycling and stabilized by π-conjugation and phenyl substituents. The CuI/Bent-NH$_2$ catalyst exhibited good recyclability, retaining substantial activity over four cycles, although a slight decline in product yield was observed due to potential catalyst deactivation or product adsorption. Comparative analysis demonstrated the superiority of this method over previously reported homogeneous systems, especially in terms of environmental friendliness, simplicity, and reusability.

## 1 Introduction

Recent years have witnessed significant breakthroughs in heterocyclic chemistry, particularly in the development of novel synthetic strategies and diverse biological applications. Among heterocyclic scaffolds, such as quinolines,[1] pyrimidines,[2] benzofurans,[3] thiophenes,[4] and thiazoles,[5] the 1,3,4-oxadiazole nucleus has been extensively investigated due to its robust biological profile. Of the four available regioisomeric forms, this specific 1,3,4-oxadiazole core has received sustained research interest to date. This preference stems from its intrinsic high chemical stability, favorable extended π-conjugation system, and superior electronic properties, which collectively make it highly attractive for materials science and medicinal chemistry applications.[6] Structurally, the 1,3,4-oxadiazole ring resembles furan, with substitution possible at the 2 and 5 positions; this
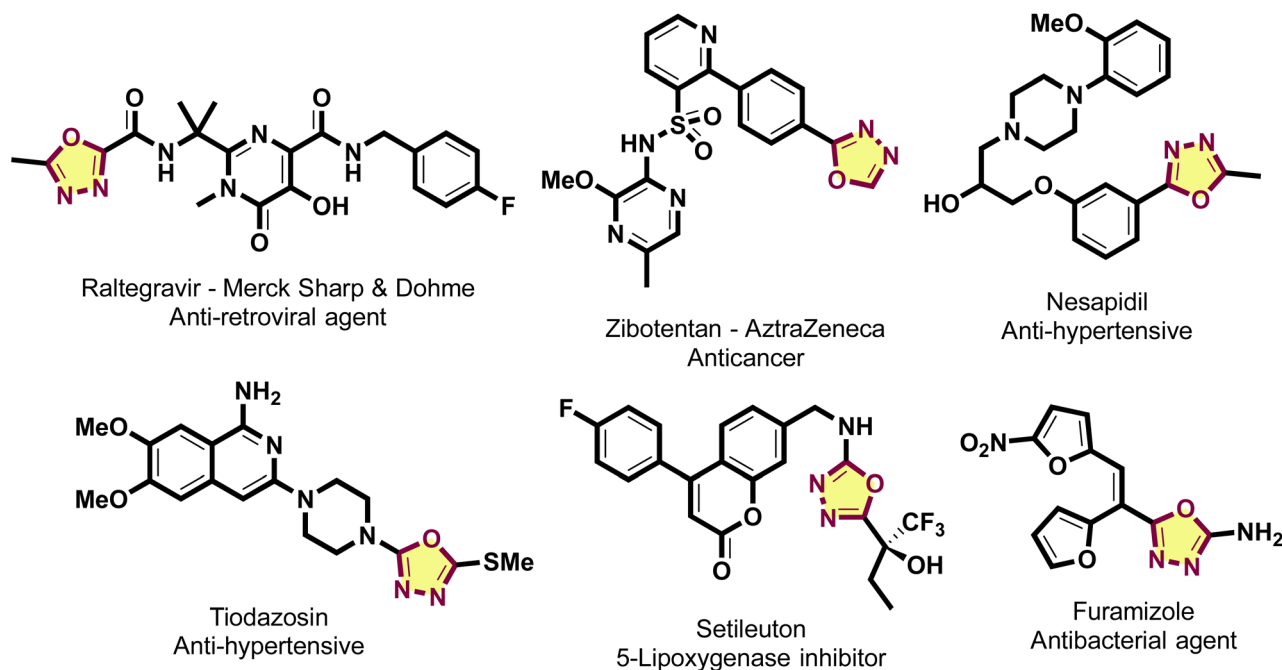
arrangement imparts excellent thermal and mechanical resilience while reducing the carbon-to-nitrogen ratio to enhance chemical stability.[6,7] In pharmacology, this scaffold is a key pharmacophore in several FDA-approved drugs, including the HIV-1 integrase inhibitor Raltegravir, the antihypertensives Nesapidil and Tiodazosin, and the antibacterial agent Furamizole.[7–9] The 1,3,4-oxadiazole moiety represents a privileged scaffold in medicinal chemistry, characterized by a broad spectrum of pharmacological profiles including anticancer, anti-inflammatory, antimicrobial, and anticonvulsant properties. Furthermore, the inherent π-conjugated architecture of these heterocycles has facilitated their integration into optoelectronic technologies, such as OLEDs and photovoltaics, as well as in the design of energetic materials.[6,7] Such structural robustness combined with synthetic flexibility renders the 1,3,4-oxadiazole core an indispensable building block for the frontiers of drug discovery and advanced functional materials (Scheme 1).

In tandem with advancements in molecular synthesis, the global transition toward green chemistry has intensified the

*Department of Organic Chemistry, Faculty of Chemistry, University of Science, Ho Chi Minh City, 700000, Vietnam. E-mail: ngthai@hcmus.edu.vn*

*Vietnam National University, Ho Chi Minh City, 700000, Vietnam*

**Scheme 1** Oxadiazole-containing molecules with therapeutic properties.

Raltegravir - Merck Sharp & Dohme
Anti-retroviral agent

Zibotentan - AztraZeneca
Anticancer

Nesapidil
Anti-hypertensive

Tiodazosin
Anti-hypertensive

Setileuton
5-Lipoxygenase inhibitor

Furamizole
Antibacterial agent

demand for sustainable, recyclable catalysts.[10] Consequently, clay minerals have emerged as promising candidates in heterogeneous catalysis due to their environmental compatibility and structural tunability. Within the diverse classifications of clays-including smectite, kaolinite, and illite-bentonite stands out; it is predominantly composed of 2 : 1-type montmorillonite, characterized by a fundamental layered architecture centered around an octahedral $Al^{3+}$ sheet.[11] The prominence of bentonite stems from its substantial specific surface area, high cation exchange capacity, and exceptional thermal stability.[12] Purified and modified bentonite has emerged as an efficient catalyst for various organic transformations, such as alkylation,[13] acylation,[14] esterification,[15] and the synthesis of heterocyclic compounds.[16,17] Its inherent reusability and commendable thermal stability further highlight bentonite's potential as a compelling, eco-friendly replacement for toxic homogeneous catalysts in sustainable chemical processes.

This study focuses on developing a sustainable synthetic methodology for 2,5-disubstituted 1,3,4-oxadiazoles, a scaffold of significant pharmaceutical potential. The strategy involves the engineering of an eco-friendly catalytic system by functionalizing bentonite with (3-aminopropyl)triethoxysilane (APTES) to serve as a robust support for CuI immobilization. This heterogeneous CuI/Bent-NH$_2$ catalyst, in combination with potassium persulfate as a 'green' oxidant, was employed to mediate the oxidative cyclization of N-acylhydrazones. Through a multi-step synthetic route, a series of 2,5-disubstituted 1,3,4-oxadiazole derivatives were successfully synthesized with consistent yields. These findings underscore the versatility and efficacy of modified bentonite as a promising material in the field of sustainable catalysis.
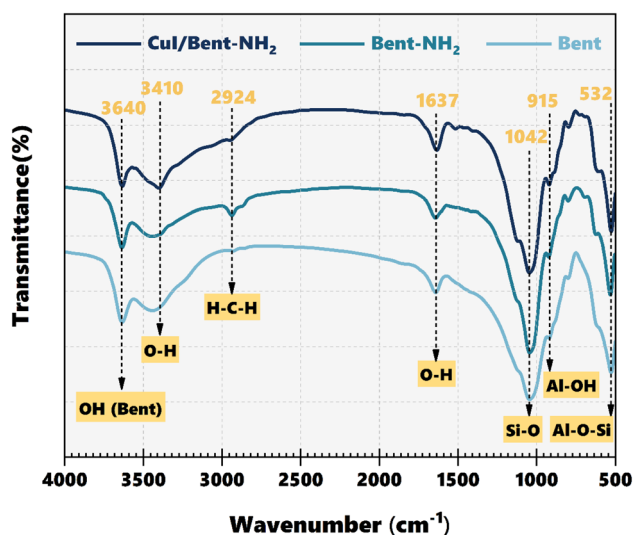
## 2 Results and discussion

### 2.1 Synthesis of CuI/Bent-NH$_2$

Scheme 2 illustrates the stepwise functionalization and metal loading process leading to the formation of CuI nanoparticles supported on amine-modified bentonite (CuI/Bent-NH$_2$).[18–20] Initially, natural bentonite (Bent) was modified with 3-aminopropyltriethoxysilane (APTES) in toluene to introduce surface amine groups, yielding amino-functionalized bentonite (Bent-NH$_2$).[20] These amine groups act as anchoring sites for copper ions. Upon treatment with an aqueous CuSO$_4$ solution (0.1 M), Cu$^{2+}$ ions were adsorbed and coordinated to the –NH$_2$ moieties through electrostatic and donor–acceptor interactions, forming Cu$^{2+}$-loaded bentonite (Cu/Bent-NH$_2$). Subsequently, the Cu$^{2+}$ species were converted to Cu$^+$ and immobilized as CuI nanoparticles by in situ reaction with KI (0.1 M). In this step, iodide ions not only served as reducing agents but also provided the I$^-$ source for CuI formation, as reported in similar Cu-based catalyst syntheses (CuI/Bent-NH$_2$).[21]

The FT-IR analysis was performed to determine the functionality of the organic matter on the catalyst and the presence of certain chemical bonds in the substrate's structure. The FT-IR spectrum of the bentonite substrate after the silane modification shows a successful grafting of silane (Fig. 1). A distinct, weak signal at 2900 to 2950 cm$^{-1}$ of the C–H bond stretching vibration of the silane's methylene carbon can be seen on the modified bentonite (Bent-NH$_2$) and the CuI-deposited modified bentonite (CuI/Bent-NH$_2$). Two medium-intensity, wide bands at 3350−3600 cm$^{-1}$ and 1600−1750 cm$^{-1}$ were attributed to the deformation and stretching of the O–H bond in water molecules within the interlayer gap. Strong absorption bands of 500–
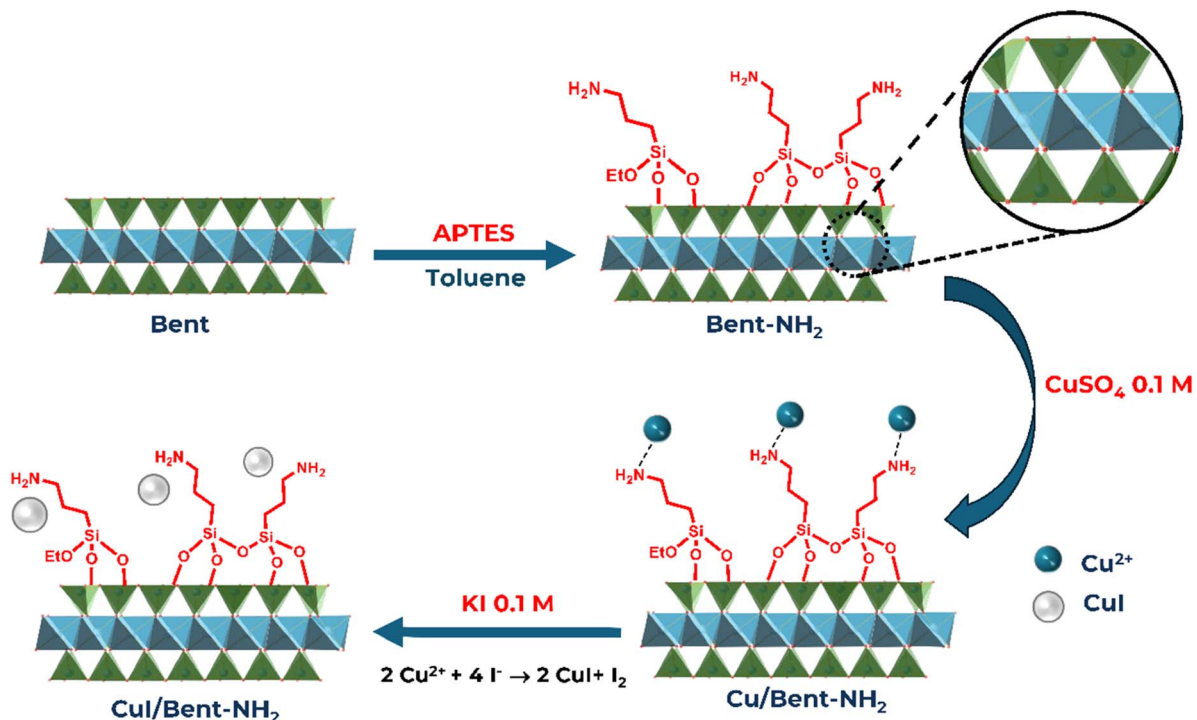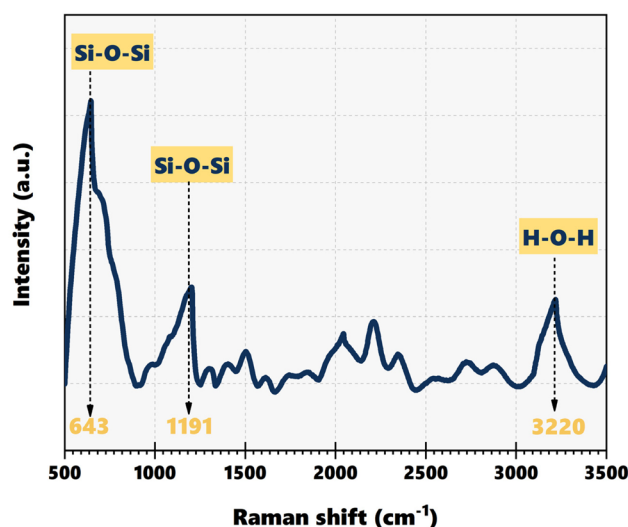
**Scheme 2** Preparation process of CuI/Bent-NH$_2$ from bentonite (Bent).



**Fig. 1** FT-IR spectra of bent, Bent-NH$_2$, and CuI/Bent-NH$_2$.

silicate structure. The broad band observed at 3220 cm$^{-1}$ was characteristic of O–H stretching vibrations, suggesting the existence of structural hydroxyl groups (–OH) and possibly interlayer water molecules. These spectral features are consistent with previously reported studies on bentonite-based or silicate materials. Madejová *et al.* reported that bentonites display strong Raman bands related to Si–O–Si vibrations between 600 and 1200 cm$^{-1}$, with additional features above 3000 cm$^{-1}$ linked to hydroxyl or adsorbed water content.[23] Furthermore, López-Galindo *et al.* highlighted that the

550 cm$^{-1}$ and 1000−1070 cm$^{-1}$ correspond to the deformation of the Al–O–Si bond and vibration of the Si–O bond.[22]

In Fig. 2, the Raman spectrum of the bentonite-based material reveals three major characteristic bands at approximately 643 cm$^{-1}$, 1191 cm$^{-1}$, and 3220 cm$^{-1}$. The strong band at 643 cm$^{-1}$ was attributed to the bending vibration of Si–O–Si bonds, which was typical of silicate frameworks such as montmorillonite, the dominant component in bentonite. The peak at 1191 cm$^{-1}$ was associated with asymmetric stretching vibrations of Si–O–Si, confirming the presence of a tetrahedral



**Fig. 2** Raman spectroscopy of CuI/Bent-NH$_2$.

hydration state and surface modifications of bentonite significantly influence the intensity of the OH-related bands in the Raman spectrum.[24]

Fig. 3 displays the XRD pattern of the CuI/Bent-NH$_2$ catalysts, revealing and confirming structural insights into both the bentonite support and the CuI phase. The diffraction peaks match closely with the standard patterns for montmorillonite (JCPDS no. 13-0135) and CuI (JCPDS no. 01-0561), confirming that both materials are present in the hybrid.[25] Three distinctive broad peaks of bentonite clay were observed at 20.17, 35.99, and 62.18°. The intact montmorillonite peaks indicated that the layered architecture of bentonite mostly remains unchanged following the incorporation of functional groups and metals. No significant alterations in peak positions or the emergence of new diffraction lines were observed, indicating that CuI was dispersed throughout the bentonite rather than intercalated between its layers.[26] The XRD pattern exhibited low-intensity but distinct peaks at 25.59° and 42.29°, corresponding to the (111) and (220) planes of crystalline CuI, respectively. These observations confirm the effective immobilization of CuI onto the amine-functionalized bentonite.[27]

Energy-dispersive X-ray spectroscopic analysis was performed to determine the elemental composition of the elements present in the catalyst (Fig. 4). The spectrum reveals distinct peaks corresponding to elements such as O, N, C, Cu, Mg, Al, Si, S, Cl, I and Ca, indicating their presence in the sample. The strong signals from oxygen and silicon, along with aluminum, confirming that the bentonite substrate is primarily composed of silicate layers. The identification of nitrogen confirms successful amine functionalization (–NH$_2$), while the copper signal supports the incorporation of Cu(I) species into the material. Additionally, the quantitative bar chart inset reinforces this observation, showing that oxygen is the most abundant element in both atomic and mass percentages, followed by silicon and aluminum, which are characteristic of aluminosilicates. The measurable nitrogen content confirms
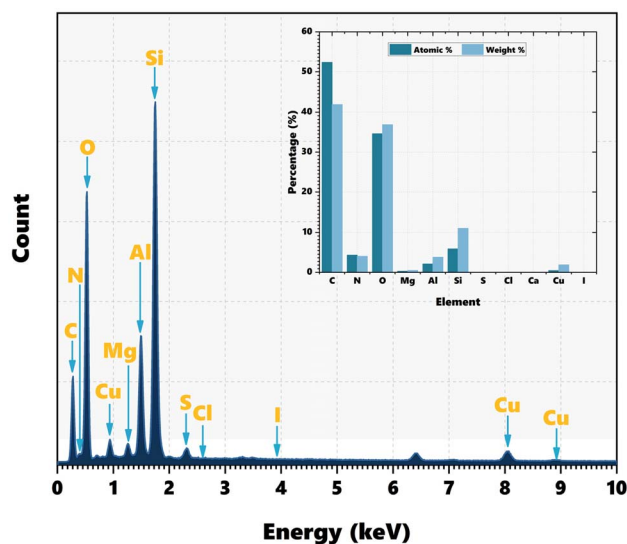


Fig. 4 EDX spectroscopy of CuI/Bent-NH$_2$.

the effective surface functionalization of the clay. The $L_\alpha$ emission line of iodine at 3.93 keV was not detected.[28] The Bent-NH$_2$ after the CuI deposition exhibited a color transition instead of the grayish-brown color of CuI.

As shown in Fig. 5, the SEM images (a–e) exhibited a typical layered and plate-like morphology of bentonite, characterized by wrinkled sheets and irregular aggregates. The particle surfaces appeared rough and porous. The particle size distribution (f) revealed that most particles range from 1.5 to 4.0 μm, with an average around 2.5–3.0 μm, following a normal distribution. This size range was consistent with mechanically processed bentonite, as reported in previous studies. These results agree with published literature, confirming that the material retains the typical structural and morphological characteristics of natural bentonite.[29]

The EDX elemental mapping images showed a uniform distribution of major elements, including Si, Al, O, Mg, and Ca, which were characteristic components of bentonite, particularly montmorillonite (Fig. 6). The presence of Si and Al indicated a layered aluminosilicate structure, while O confirmed the oxide nature of the material. The presence of Mg and Ca suggested substitution within the clay layers or cation exchange, which was commonly observed in natural bentonite. The relatively homogeneous distribution of Cu demonstrated the successful loading or functionalization of the metal onto the bentonite surface. The detection of C and N could be due to organic functional groups or surface modification. These findings aligned with prior studies; Madejová et al. confirmed that natural bentonites exhibit strong signals for Si, Al, O, and variable levels of Mg and Ca, while surface-modified clays may show additional heteroatoms such as N, S, or transition metals depending on treatment.[30] Similarly, research by Zhu et al. on metal-functionalized clays reported successful and uniform incorporation of Cu on the bentonite surface for enhanced catalytic applications.[31]
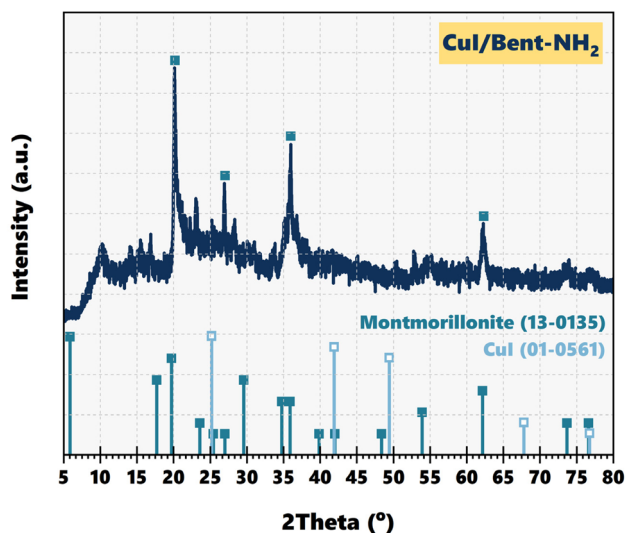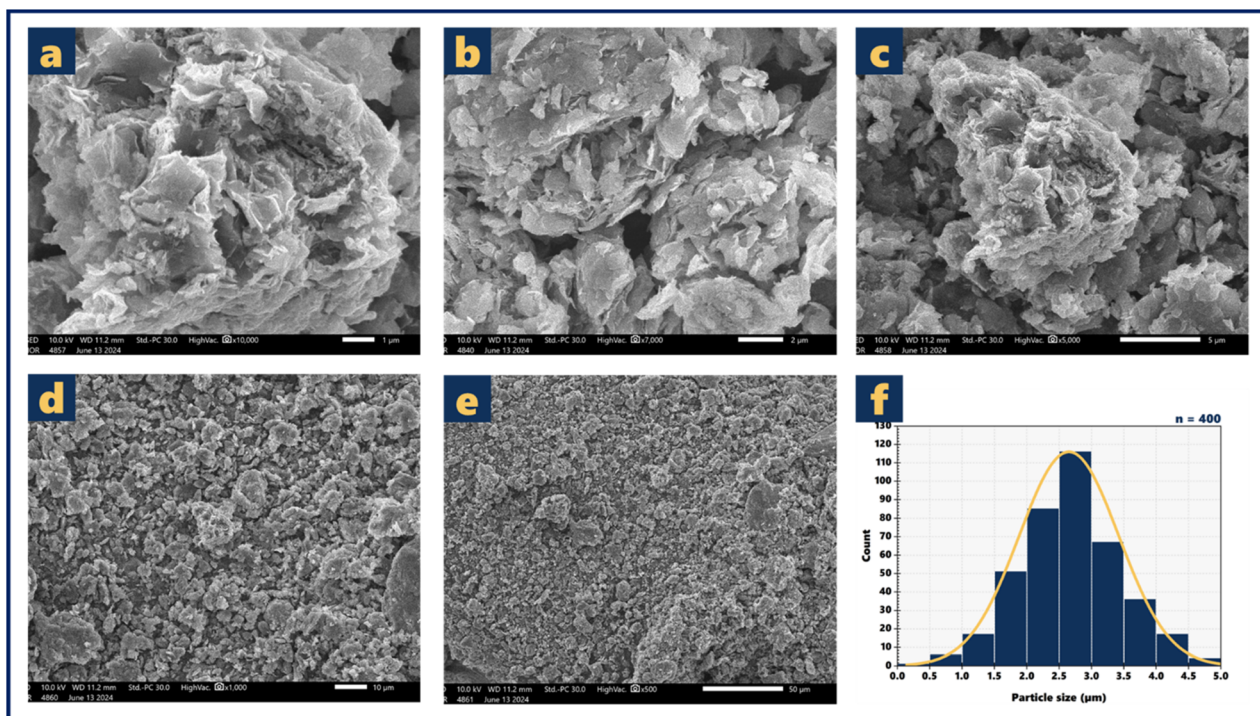


Fig. 3 XRD pattern of CuI/Bent-NH$_2$.

**Fig. 5** SEM photographs at 1 μm (a), 2 μm (b), 5 μm (c), 10 μm (d), 50 μm (e), and particle size graph of CuI/Bent-NH$_2$ (f).

According to Fig. 7, the BET isotherm (left) showed a well-defined linear region in the relative pressure range of 0.05–0.30, yielding a calculated BET specific surface area of 20.13 m$^2$ g$^{-1}$. The adsorption isotherm (right) showed a steep uptake at low relative pressures, indicating the presence of micropores, followed by a gradual increase typical of mesoporous structures. The average pore diameter was 20.85 Å (2.08 nm), classifying the material within the mesoporous range.[32] Additionally, the t-plot micropore volume was 0.001479 cm$^3$ g$^{-1}$, suggesting a small fraction of micropores within the structure. These values were consistent with previous reports on bentonite-based materials, which typically exhibited surface areas ranging from 10 to 60 m$^2$ g$^{-1}$ depending on treatment and functionalization.[33,34]

The thermogravimetric analysis (TGA) of the CuI/Bent-NH$_2$ material exhibited a multi-stage weight loss pattern as the temperature increases from 50 °C to 600 °C (Fig. 8). An initial weight loss of 3.6% below 150 °C was attributed to the evaporation of physically adsorbed moisture. A subsequent weight loss of approximately 4.7% was recorded between 150 and 250 °C, corresponding to the removal of interlayer water. Additional losses of 1.9% (250−350 °C) and 2.0% (350−450 °C) likely resulted from dehydroxylation of structural –OH groups in the clay layers. A further 5.0% weight loss from 450–600 °C could be associated with the decomposition of residual organic compounds or irreversible structural changes. This decomposition profile was consistent with previously reported behavior of natural and modified bentonite clays, which typically showed dehydration and dehydroxylation steps across this temperature range.[35]

The survey X-ray photoelectron spectroscopy XPS spectrum of the prepared catalyst confirmed the presence of elemental constituents corresponding to Al, Si, C, O, N, Cu, and I. Subsequent high-resolution deconvolution of the core-level spectra (Al 2p, Si 2p, O 1s, C 1s, N 1s, Cu 2p, and I 3d) was performed to characterize the chemical states and interatomic bonding environments within the material matrix. The Al 2p spectrum (Fig. 9f) evidenced the existence of aluminol (Al–OH), characterized by a binding energy (BE) of 74.8 eV. Furthermore, the predominant form of Al atoms was attributed to the aluminum-oxygen (Al–O) bond at a BE of 73.7 eV.[36] For the Si 2p spectrum (Fig. 9e), the BE for silanol (Si–OH) was located at 103.4 eV. Crucially, the magnitude of the Si–OH bond signal was significantly attenuated compared to the silicon-oxygen linkages (Si–O–Si or Si–O–Al), which were prominently observed at approximately 102.5 eV. The Si 2p envelope also displayed an overlapping signal corresponding to the Si–O–C bond originating from the ethoxy groups in APTES.[37] Definitive evidence for the successful chemical grafting of APTES onto the bentonite was provided by the O 1s spectrum (Fig. 9c). A strong, characteristic component at 531.8 eV was attributed to the Si–O bond present in both the bentonite framework and the APTES moiety. Additionally, lower intensity signals were resolved in the O 1s region at 530.8 eV (Al–O) and 529.8 eV (O lattice). The successful immobilization of APTES was further corroborated by the N 1s spectrum (Fig. 9d), which distinctly resolved three unique chemical states of nitrogen: C–NH$_2$ (399.5 eV), C–NH$_3^+$ (401.2 eV), and C–N (403.3 eV).[37] Analysis of the C 1s spectrum (Fig. 9b) revealed signals at 284.2 eV and 284.8 eV, originating from the C–Si and C–C/C═C bonds within the material's framework.[38] The peaks resolved at 292.8 eV and 295.6 eV were assigned to π–π* transitions, which is likely indicative of residual toluene physisorbed onto the bentonite structure. The
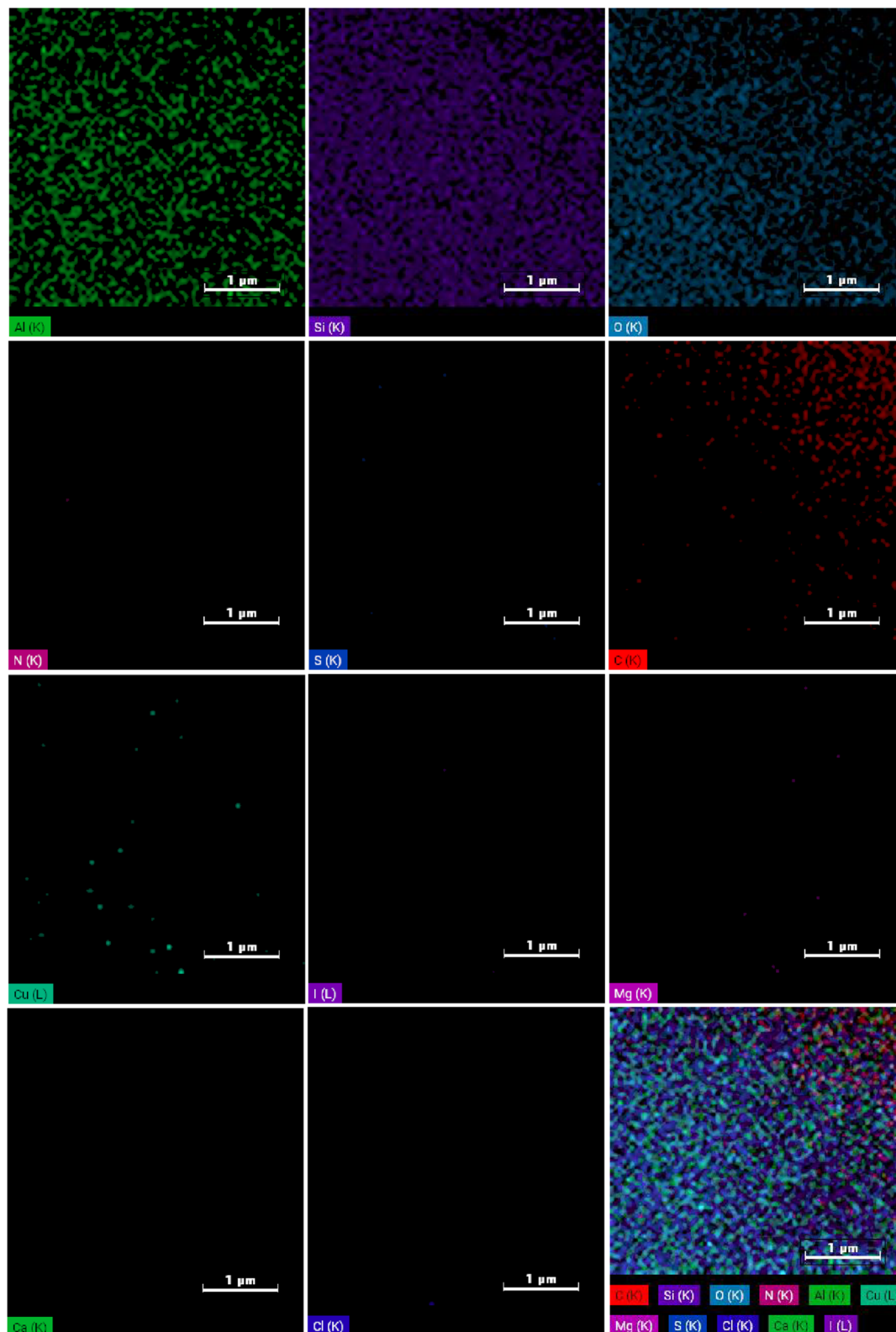
Fig. 6 EDX mapping of CuI/Bent–NH$_2$.
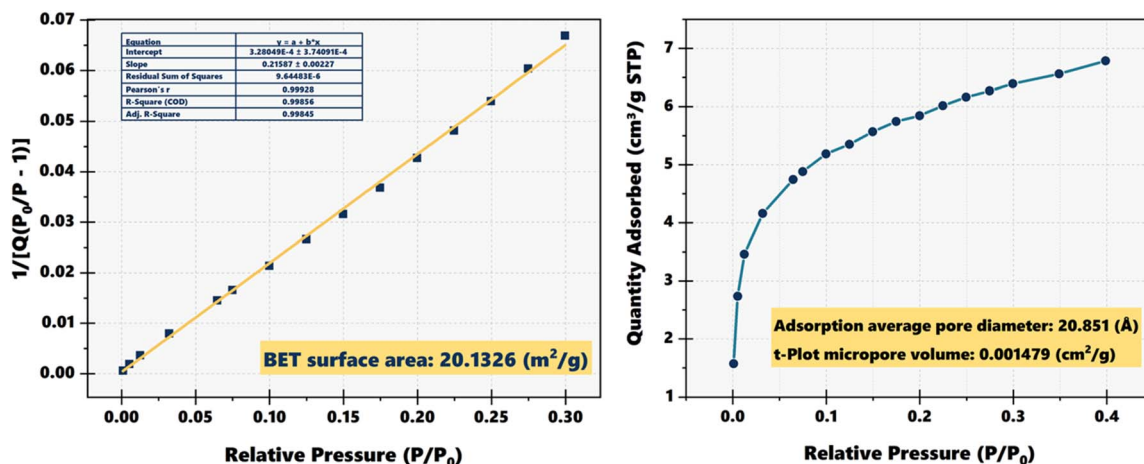
incorporation of copper(I) iodide onto the bentonite support was unequivocally demonstrated through the Cu 2p and I 3d XPS spectra (Fig. 9g and h). For Cu 2p, the spin-orbit doublet at 932.0 eV and 951.8 eV were designated as the Cu 2p$_{3/2}$ and Cu 2p$_{1/2}$ signals, respectively. These binding energies are characteristic of Cu$^+$ species. Notably, the absence of shake-up satellite

Fig. 7 BET of CuI/Bent-NH$_2$.
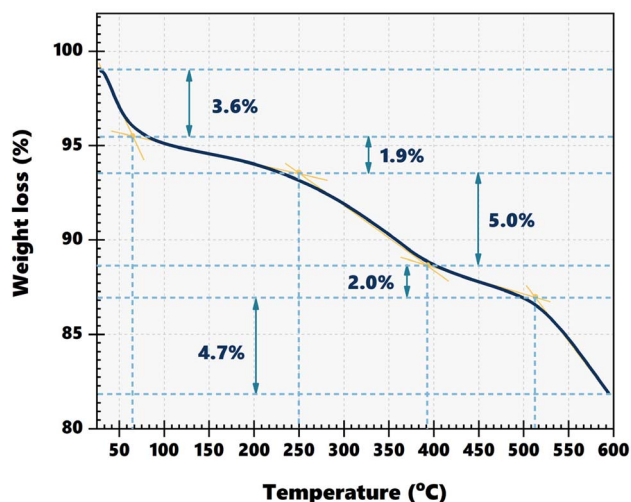


Fig. 8 TGA curve of CuI/Bent-NH$_2$.

peaks in the 940–945 eV range confirms that no $Cu^{2+}$ exists in the sample.[39] Similarly, the I 3d spectrum presented characteristic binding energy peaks at 620.0 eV and 630.3 eV, representative of the I $3d_{3/2}$ and I $3d_{5/2}$.[40]

ICP-MS analysis determined the Cu content (active catalytic sites) to be 0.69 mmol g$^{-1}$ (Table 1).

## 2.2 Synthesis of 2,5-disubstituted-1,3,4-oxadiazoles

This work describes the multi-step synthetic pathway for the construction of a 2,5-disubstituted-1,3,4-oxadiazole compound, starting from benzoic acid (Scheme 3). The procedure commences with an esterification reaction involving benzoic acid and methanol, facilitated by 98% sulfuric acid at 120 °C for 6 h, resulting in a 49% yield of methyl benzoate.[41] This ester was then treated with hydrazine hydrate ($N_2H_4$) and potassium hydroxide (KOH) at 130 °C for 8 h to form a benzohydrazide compound intermediate with a 76% yield.[42] In the next step, benzohydrazide was introduced into benzaldehyde and ethanol

under reflux conditions to form the hydrazone derivatives with a 96% yield.[43,44] Finally, the compound undergoes intramolecular cyclization in the presence of a heterogeneous CuI/ Bent-NH$_2$ catalyst system, along with $K_2CO_3$ and $K_2S_2O_8$ in DMSO at 100 °C for 8 h, affording the target 2,5-disubstituted-1,3,4-oxadiazole derivative in good yield. This synthetic sequence highlights an efficient and environmentally friendly route for the construction of heterocyclic scaffolds, leveraging a recoverable, solid-supported catalyst.

Table 2 illustrates that an examination of reaction temperature revealed a correlation between increasing temperature and product yield (Entries 1–5, Table 2). The product yield is meager at room temperature (3%) with a low increment at 60 °C (6%). At 80 °C, the yield rapidly increases to 16%. The reaction yield was a mere 18% and 19% at 100 °C and 120 °C, respectively. At 120 °C, the reaction mixture formed a viscous brown residue and TLC spotting of the reaction mixture showed a streak of brown-green hue of unknown side products stretching from the origin to near the product spot. The reaction temperature of 100 °C was chosen to investigate the molar equivalent of potassium persulfate (Entry 4, Table 2). Without potassium persulfate, no product was detected when using TLC (Entry 6, Table 2). The product yield exhibited a substantial rise from 18% to 32% when 2 equivalents of potassium persulfate were utilized in comparison to 1 equivalent (Entries 4 and 7, Table 2). This increase in yield may result from the exposed surface of potassium persulfate crystals that can release persulfate ions into the reaction medium. The breakdown of persulfate ions will form sulfate ions that can crystallize with the potassium ions in the saturated reaction medium, depositing on the potassium persulfate crystals and blocking the further release of persulfate ions. When 3 equivalents of potassium persulfate were used (Entry 8, Table 2), the reaction mixture began to self-heating after being heated for 1 minute and releasing colorless gas profusely, the TLC analysis showed no product was formed and the hydrazone spot also diminished and replaced by a continuous streak of unidentified products. The potent oxidizing properties of potassium persulfate may
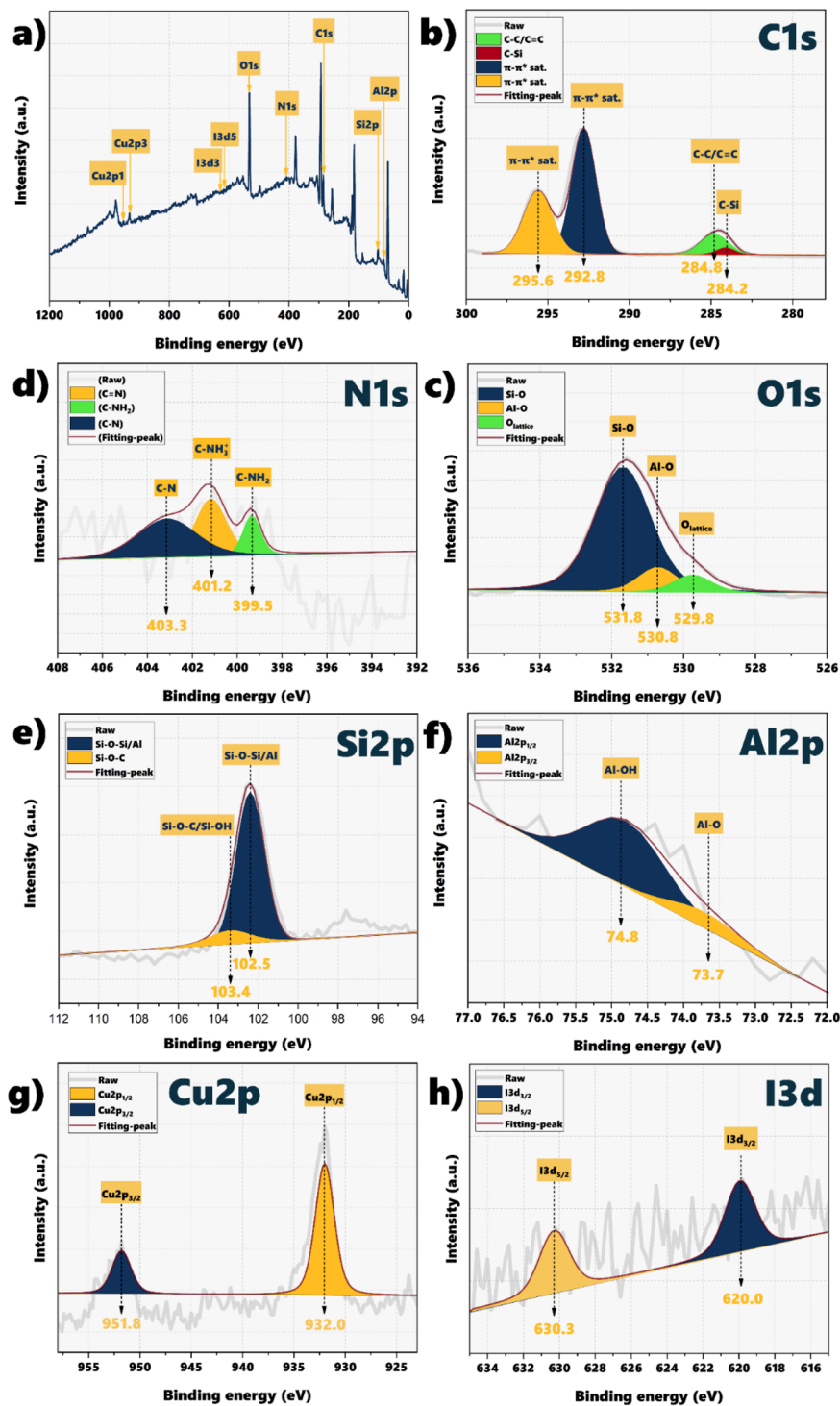
**Fig. 9** XPS spectrum of CuI/Bent-NH$_2$ catalyst with (a) survey XPS spectra, high-resolution XPS spectra of (b) C 1s; (c) O 1s; (d) N 1s; (e) Si 2p; (f) Al 2p; (g) Cu 2p; and (h) I 3d.

**Table 1** ICP-MS analysis results

| Sample | Cu content (mmol g$^{-1}$) |
| --- | --- |
| Bent-NH$_2$ | 0.03 |
| CuI/bent-NH$_2$ | 0.72 |

impose a restricted limit on the potassium sulfate/hydrazone ratio applicable for oxidizing the hydrazone to the 1,3,4-oxa-diazole product, beyond which uncontrollable oxidation prevails as the primary reaction. A 1 : 2 molar ratio of hydrazone to oxidizer would be ideal for the oxidative cyclization of hydrazone. When TBHP was used in place of potassium
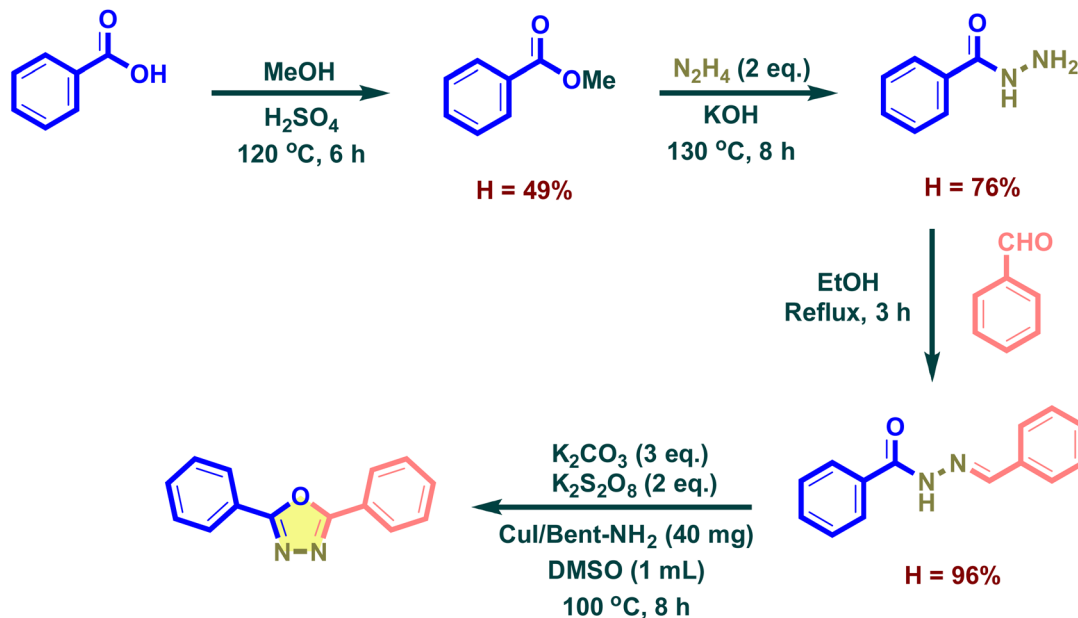
**Scheme 3** Preparation of 2,5-disubstituted-1,3,4-oxadiazoles.

**Table 2** Reaction condition optimization[a]



| Entry | Temp. (°C) | Oxidation reagents | Loading of oxidation reagents (eq.) | Solvents[b] | Loading of CuI/Bent-NH$_2$ (mg mmol$^{-1}$) | Time (h) | Isolated yield[c] (%) |
|---|---|---|---|---|---|---|---|
| 1 | RT | K$_2$S$_2$O$_8$ | 1 | DMSO | 40 | 8 | 3 |
| 2 | 60 | K$_2$S$_2$O$_8$ | 1 | DMSO | 40 | 8 | 6 |
| 3 | 80 | K$_2$S$_2$O$_8$ | 1 | DMSO | 40 | 8 | 16 |
| 4 | 100 | K$_2$S$_2$O$_8$ | 1 | DMSO | 40 | 8 | 18 |
| 5 | 120 | K$_2$S$_2$O$_8$ | 1 | DMSO | 40 | 8 | 19 |
| 6 | 100 | K$_2$S$_2$O$_8$ | 0 | DMSO | 40 | 8 | NR[d] |
| 7 | 100 | K$_2$S$_2$O$_8$ | 2 | DMSO | 40 | 8 | 32 |
| 8 | 100 | K$_2$S$_2$O$_8$ | 3 | DMSO | 40 | 8 | NR[d] |
| 9 | 100 | TBHP | 2 | DMSO | 40 | 8 | 17 |
| 10 | 100 | K$_2$S$_2$O$_8$ | 2 | Sulfolane | 40 | 8 | 5 |
| 11 | 100 | K$_2$S$_2$O$_8$ | 2 | DMF[e] | 40 | 8 | 11 |
| 12 | 100 | K$_2$S$_2$O$_8$ | 2 | ACN[e] | 40 | 8 | 28 |
| 13 | 100 | K$_2$S$_2$O$_8$ | 2 | None | 40 | 8 | NR[d] |
| 14 | 100 | K$_2$S$_2$O$_8$ | 2 | DMSO | 0 | 8 | 18 |
| 15 | 100 | K$_2$S$_2$O$_8$ | 2 | DMSO | 10 | 8 | 27 |
| 16 | 100 | K$_2$S$_2$O$_8$ | 2 | DMSO | 20 | 8 | 31 |
| 17 | 100 | K$_2$S$_2$O$_8$ | 2 | DMSO | 60 | 8 | 30 |
| 18 | 100 | K$_2$S$_2$O$_8$ | 2 | DMSO | 40 | 1 | 26 |
| 19 | 100 | K$_2$S$_2$O$_8$ | 2 | DMSO | 40 | 2 | 27 |
| 20 | 100 | K$_2$S$_2$O$_8$ | 2 | DMSO | 40 | 3 | 29 |
| 21 | 100 | K$_2$S$_2$O$_8$ | 2 | DMSO | 40 | 4 | 30 |
| **22** | **100** | **K$_2$S$_2$O$_8$** | **2** | **DMSO** | **40** | **5** | **32** |
| 23 | 100 | K$_2$S$_2$O$_8$ | 2 | DMSO | 40 | 6 | 31 |
| 24 | 100 | K$_2$S$_2$O$_8$ | 2 | DMSO | 40 | 7 | 32 |
| 25 | 100 | K$_2$S$_2$O$_8$ | 2 | H$_2$O | 40 | 5 | 8 |
| 26 | 100 | K$_2$S$_2$O$_8$ | 2 | EtOH | 40 | 5 | NR[d] |

[a] Reaction conditions: hydrazone (1 mmol), oxidation reagents (1–3 eq.), solvents (1 mL), CuI/Bent-NH$_2$ (0–60 mg mmol$^{-1}$). [b] Volume of solvent: 1 mL. [c] Isolated yield was recorded by column chromatography with *n*-hexane : ethyl acetate = 98 : 2. [d] NR = No reaction. [e] DMF = Dimethylformamide, ACN = Acetonitrile.

persulfate (Entry 9, Table 2), the product yield was lower, this can be explained by the reduction potential of TBHP being much lower compared to that of persulfate, hence lower oxidizing power.[45] The investigation of solvents was performed with solvents with a wide potential window (Entry 10–12, Table 2) so the oxidation of the solvent would likely not have happened and consumed the persulfate.[46,47] The process utilizing sulfolane had the lowest yield among the four solvents employed; the hydrazone was scarcely soluble in sulfolane, and upon completion of the reaction, residual hydrazone crystals were observable (Entry 10, Table 2). The solubility of the hydrazone may suggest that the reaction would likely take place in a homogeneous medium. When DMF was used (Entry 11, Table 2), the solvent turned light green quickly after being added to the solid mixture. Even though the hydrazone seemed to be dissolved completely, the yield was lower at one-third of that of entry 7, this may be due to the copper ions on the modified bentonite surface forming the copper-amine complex

with the DMF molecules. Guin *et al.* hypothesized that the coordination of the hydrazone intermediate with the copper ion would promote the cyclization and form the new carbon-oxygen bond.[48] The copper ions may have a greater affinity for DMF than the hydrazone, which hindered the hydrazone intermediate from coordinating and initiating the cyclization process, hence lowering the product yield. When using ACN as the solvent, 10 mL of ACN was used to *1)* Allow the magnetic stir bar to work due to the potassium carbonate and potassium persulfate forming a thick slurry when 1 mL of ACN was used; *2)* To compensate for the volume of ACN that constantly refluxing because the experiment setup required a condenser and the volatile nature of ACN makes it likely to evaporate off the reaction vessel over the course of 8 h. The product yield was satisfactory at 28%; however, the intrinsic complexity of the reaction setup and the utilization of tenfold the solvent volume compared to entry 7 rendered entry 12 unfavorable for examining the other conditions. Using the condition of entry 7, the
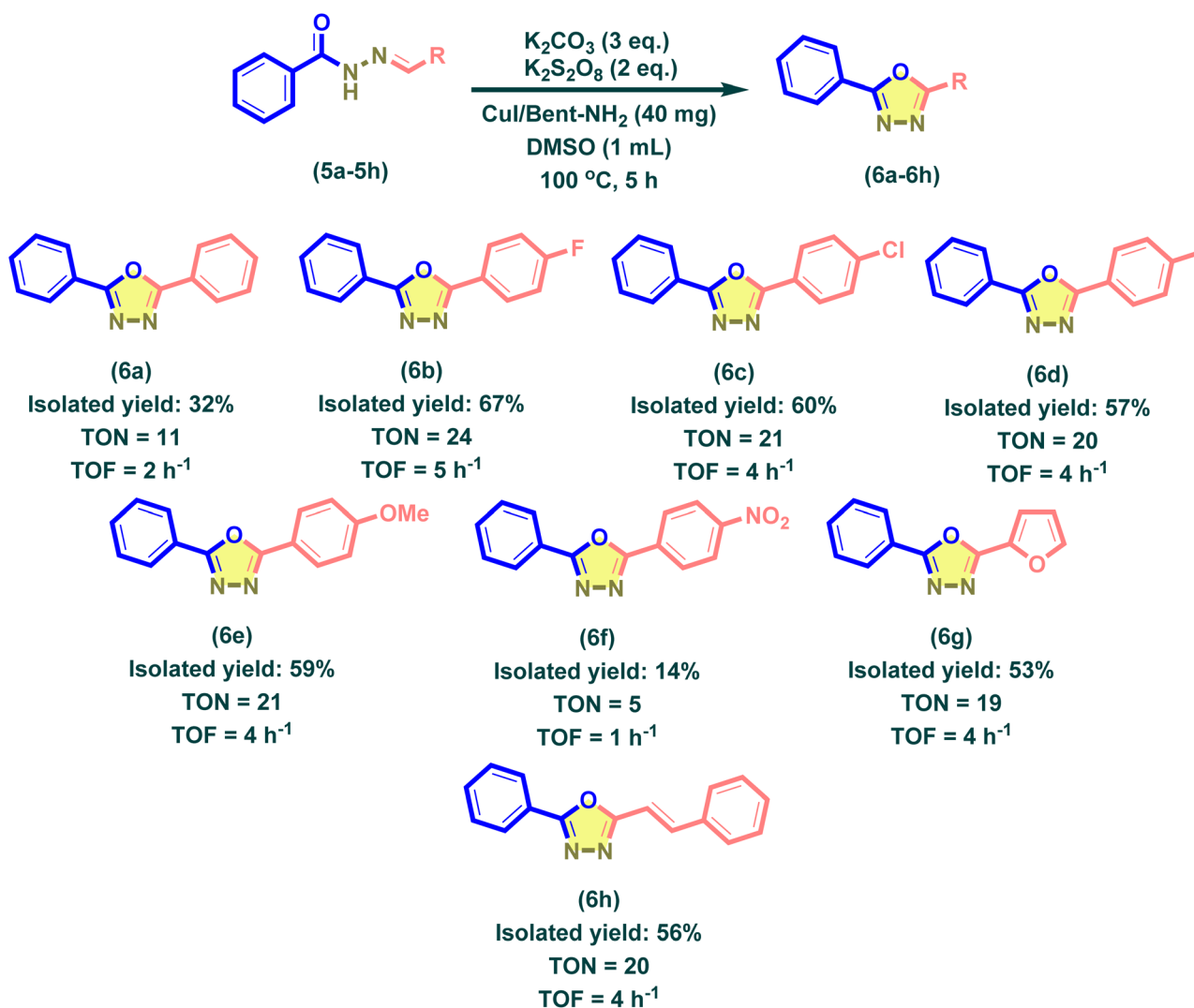


**Scheme 4** Scope of 2,5-disubstituted-1,3,4-oxadiazole derivatives. [a]Reaction conditions: hydrazone (1 mmol), $K_2CO_3$ (3 eq.), $K_2S_2O_8$ (2 eq.), CuI/Bent-NH₂ (40 mg), and DMSO (1 mL), at 100 °C for 5 h. The crude residue was purified by flash column chromatography. TON = (mole of products)/(mole of catalyst); TOF = TON/hour (h$^{-1}$).

catalyst-to-hydrazone ratio was investigated. With no catalyst being used, the **6a** product was still able to form, but with a lower yield than other experiments that used CuI/Bent-NH$_2$, the DMSO may contribute to the stability of the hydrazone intermediate. Entries 15, 7, and 16 show a low increase in yield from 31% to 32% and decrease down to 30%, respectively. The increase in yield can be related to the increase in the amount of CuI/Bent-NH$_2$ being used (Entries 7 and 15, Table 2). The decline in yield was hypothesized as the product being adsorbed in the modified bentonite support (Entry 16, Table 2). The amount of CuI/Bent-NH$_2$ used in Entries 15 and 7 was low enough so that the adsorption of **6a** was not too obvious due to the substrate being saturated with other components in the reaction mixture when water was added to quench the reaction. In entry 16, more CuI/Bent-NH$_2$ was used, so the substrate was less saturated, so a noticeable amount of **6a** would be adsorbed, contributing to the decrease in yield. The investigation of the reaction time of Entries 17 to 23 shows a similar result to the qualitative reaction using the original reaction condition. After 5 h, the product yield reached the maximum and further reaction would not increase the yield past 32%.

From Scheme 4, the yield of the 4-substituted phenyl derivatives was moderate, ranging from 14% to 67%. The **6a** and **6d** products were quite similar in their physicochemical properties but had widely different yields of 32% and 57% respectively,

which corresponds to the fact that the hydrazone **5d** dissolved readily when DMSO was added to the reaction mixture, whether in the case of the hydrazone **5a** only dissolved after the reaction mixture was heated. An increase in yield when the substituent of the phenyl group is connected to an electron-donating group (compound **6b**, **6c**, **6e**) is observed. The proposed mechanism for the oxidative cyclization of the hydrazone hypothesized the formation of a carbene from the carbon atom of the aldehyde part. The electron-rich phenyl group would increase the electron density of the carbene, making it more stable, which in turn increases the likelihood of the intermediate to undergo intramolecular cyclization and form the 1,3,4-oxadiazole ring. In the case of compound **6f**, the electron-deficient phenyl group would likely destabilize the carbene intermediate, causing a dramatic reduction in yield (14%). The catalytic efficiency across the synthesized derivatives was evaluated based on the respective turnover number (TON) and turnover frequency (TOF) values. Derivative **6b** exhibited the most prominent results, achieving a maximum TON of 24 and a TOF of 5 h$^{-1}$, which are considered satisfactory for laboratory-scale benchmarks. Conversely, derivative **6f** showed the lowest activity, with a TON of 5 and a TOF of 1 h$^{-1}$. Overall, the recorded ranges (TON = 5–24; TOF = 1–5 h$^{-1}$) indicate a relatively stable catalytic performance. These findings establish a promising
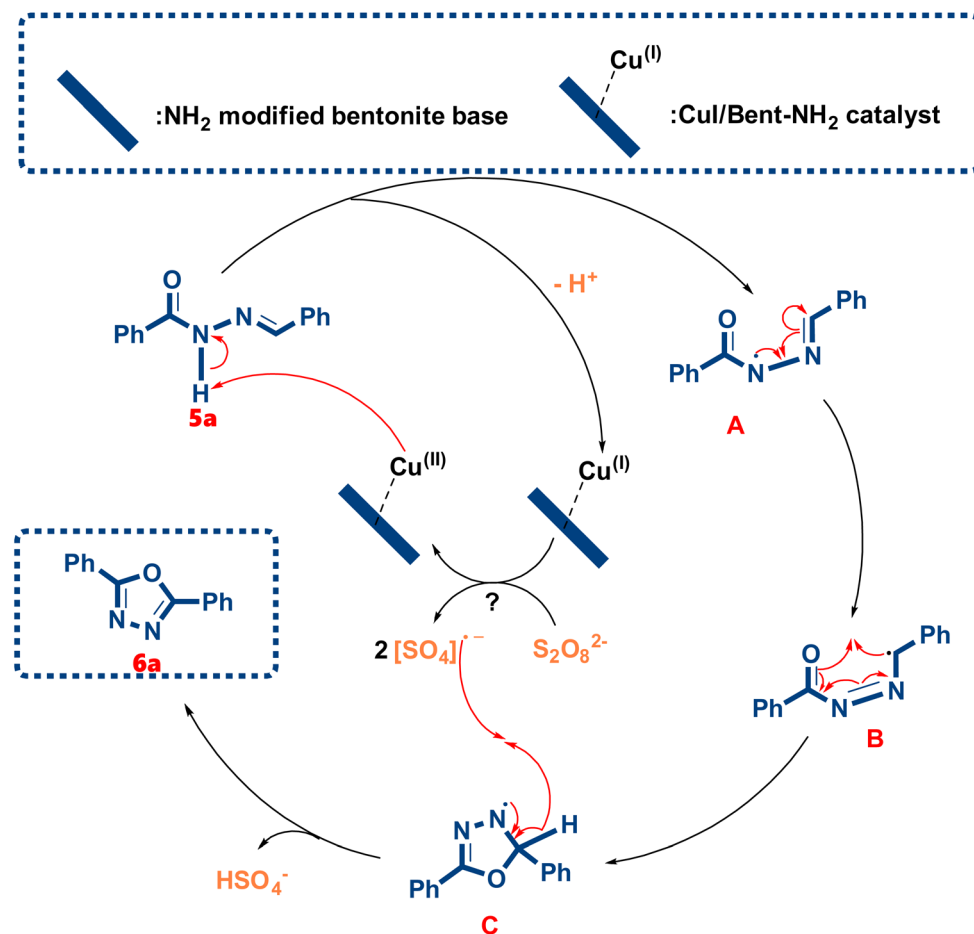


**Scheme 5** Proposed mechanism for the formation of compound **6a**.

baseline for further structural optimization and future development of this heterogeneous system.

## 2.3 Proposed mechanism for the synthesis of (6a)

From Scheme 5, the formation of compound **6a** was proposed by a mechanism with 5 steps. The reaction begins with the N–H bond being oxidized by the copper(II) ion, forming the corresponding nitrogen-radical and releasing a proton. The N–N bond is then rotated 180° to form intermediate A. The resonance of the ˙N–N=C structure of intermediate A resulted in the formation of intermediate B with the S-*cis* conformation of the carbonyl C=O and N=N double bond. Intermediate B was a benzylic radical which would be stabilized by the resonance of the phenyl group, increasing the likelihood of forming the C–O bond with the oxygen of the carbonyl and close the 5-membered ring, forming the C intermediate. The sulfate radical anion is then abstracting the hydrogen at the benzylic position, and the radical is combined with the electron of the cleaving C–H bond to form the double bond. And the sulfate radical anion was created by the homolytic cleavage of the O–O bond of the persulfate anion when heat was applied. The copper ion in the catalyst would be reoxidized by the sulfate radical cation and re-enter the oxidation cycle.[49,50]

## 2.4 Assessment of green metrics

In the context of Green Chemistry, the validation of a novel synthetic protocol's environmental compatibility is a critical prerequisite. This is accomplished by evaluating key green metrics, with specific calculation methodologies detailed in the supplementary material. The synthesis exhibited an impressively low *E*-factor of 0.51, indicating a minimal and acceptable level of waste generation. Furthermore, the low Process Mass Intensity (PMI) of 8.35 confirms highly efficient utilization of bulk materials. For this transformation, the process achieves an outstanding atom economy (AE) of 98.34%. This inherently high value signifies that nearly all atoms from the starting materials are incorporated into the final product structure. However, the reaction mass efficiency (RME) is moderate at 65.89%. This observation suggests that although the reaction mechanism is highly efficient (high AE), the actual chemical yield of the transformation is the primary factor limiting the

overall RME. The procedure further demonstrates a good carbon efficiency (CE) of 67.0%, and an acceptable eco-score of 66.5%, collectively validating the overall feasibility and sustainability of the developed methodology.[51–53]

## 2.5 Reusability of the CuI/Bent-NH$_2$ catalyst in the synthesis of (6a)

From Fig. 10, the FT-IR spectra of CuI/Bent-NH$_2$ before and after catalytic reuse reveal changes in the functional groups that reflect the material's structural stability. In the fresh catalyst, strong absorption bands at 3784, 3631, and 3412 cm$^{-1}$ correspond to Al–OH and O–H stretching vibrations, indicating the presence of structural hydroxyls and interlayer water. After reuse, these bands become weaker and broader, suggesting a partial loss of hydroxyl functionality or surface hydration, likely due to repeated heating and washing processes during recovery. These spectral changes correlate well with the catalyst recovery and product yield data. While the catalyst retains high recovery efficiency (up to 84% for the third cycle), the product yield gradually decreases from 31% to 22% after four cycles, indicating progressive catalyst deactivation. This could be attributed to surface modification or active site blockage, as evidenced by the reduced intensity of O–H and Al–OH bands in the reused material.[54]

XRD analysis was performed on the recovered catalyst to evaluate its structural stability. The resulting diffraction patterns were indexed against standard references for montmorillonite (JCPDS no. 13-0135) and CuI (JCPDS no. 01-0561). The diffractogram exhibited characteristic reflections of bentonite at $2\theta = 16.87°, 20.10°, 35.66°, 37.32°, 54.84°$, and 62.09°, confirming that the silicate framework remained largely intact following the recycling cycles. A low-intensity peak observed at 25.51° corresponds to the presence of CuI, though its significantly diminished magnitude suggests a notable loss of the active phase after recovery. Consequently, the yield of product **6a** experienced a gradual decline from 31% to 22% over four consecutive catalytic runs.

## 2.6 Comparison of this work to various synthetic methods

The comparison of various synthetic methods for constructing 2,5-disubstituted-1,3,4-oxadiazole frameworks, as summarized
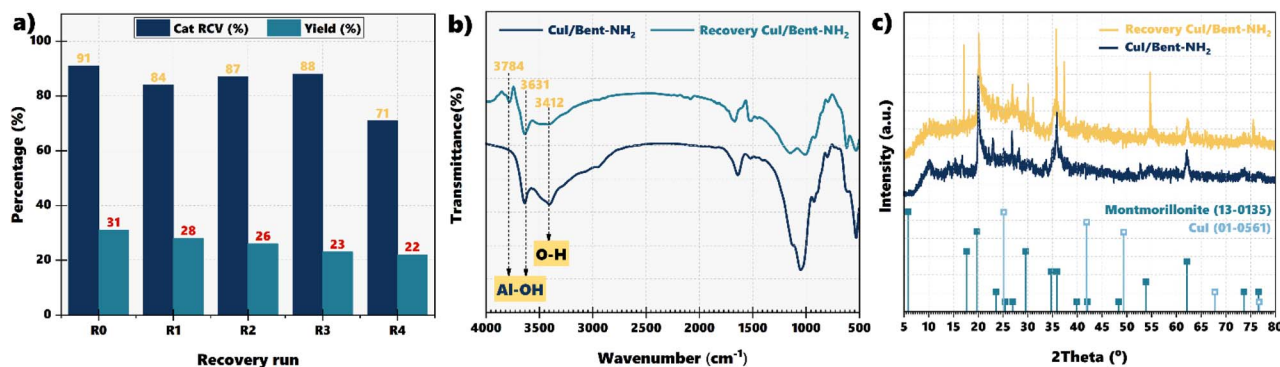


**Fig. 10** Catalytic activity of CuI/Bent-NH$_2$ in four cycles for the reaction of **6a** (A); FT-IR spectra of CuI/Bent-NH$_2$ fresh and CuI/Bent-NH$_2$ recovery (B); XRD pattern of CuI/Bent-NH$_2$ fresh and CuI/Bent-NH$_2$ recovery (C).

in Table 3. Traditional multi-step syntheses, such as the method using (*t*-Butoxycarbonyl)phenylalanine with SOCl$_2$ and pyridine, offer relatively low yield (30%) and require complex procedures. More efficient approaches, such as the one employing KI/UHP/ K$_2$CO$_3$ under mild conditions (0 °C, DME-H$_2$O), achieve a higher yield of 70% but require long reaction times (20 h). The method utilizing ceric ammonium nitrate with benzohydrazide and 4-methoxybenzaldehyde also affords a good yield (67%) under reflux in CH$_2$Cl$_2$, though it requires extended reaction time (11 h). The highest reported yield (73%) was obtained *via* a CDI-mediated reaction with benzoyl hydrazide and pivalic acid under mild conditions (0 °C), highlighting the efficiency of this approach. The method reported in this work uses a heterogeneous CuI/Bent-NH$_2$ catalyst system, with K$_2$CO$_3$ and K$_2$S$_2$O$_8$ as additives in DMSO at 100 °C. This approach provides a competitive yield of 67% and has the added advantage of employing a reusable solid-supported catalyst, potentially offering greater environmental and operational benefits.

## 3 Experimental

### 3.1 Synthesis of CuI/Bent-NH$_2$

**3.1.1 Modification of bentonite clay with APTES.** APTES-functionalized bentonite was synthesized following the method described by Kostenko *et al.*[22] Bentonite powder (4.00 g) was suspended in toluene (10 mL) and refluxed for 2 h in a 100 mL round-bottom flask. Subsequently, a solution of APTES (1.77 g, 8 mmol) in toluene (5 mL) was added, followed by a 5 mL toluene rinse to ensure quantitative transfer (total volume: 20 mL). The mixture was refluxed for an additional 6 h with periodic agitation to maintain a homogeneous suspension and prevent clay aggregation. Upon cooling to room temperature, the solid was isolated by centrifugation. To ensure complete removal of residual toluene, the modified clay was soaked in methanol (10 mL) for 2 h, followed by centrifugation. The resulting Bent-NH$_2$ was dried at 100 °C for 12 h and pulverized using a glass mortar and pestle.

**3.1.2 Depositing copper(I) iodide on modified bentonite surface.** The synthesis of the CuI/Bent-NH$_2$ composite followed a modified procedure reported by Myeni *et al.*[59] Briefly, CuSO$_4$·5H$_2$O (0.375 g, 2 mmol) was dissolved in 20 mL of deionized water to yield a 0.1 M solution. Modified bentonite (3.00 g) was slowly introduced to the solution and stirred for 15 min to facilitate the adsorption of Cu$^{2+}$ ions onto the substrate. Subsequently, 4.5 mL of 0.1 M KI was added dropwise

over 3 h under continuous stirring. In this *in situ* process, iodide ions acted as both a reducing agent (converting Cu$^{2+}$ to Cu$^+$) and a precipitant, resulting in the nucleation and growth of CuI crystals on the bentonite surface. The resulting slurry was centrifuged, and the solid was washed with deionized water (10 mL) and allowed to equilibrate for 4 h to ensure the removal of loosely bound ions. After further centrifugation, the material underwent solvent exchange with acetone (3 × 10 mL) to remove residual water. Finally, the CuI/Bent-NH$_2$ product was dried at 100 °C for 12 h.

### 3.2 Synthesis of 2,5-disubstituted-1,3,4-oxadiazoles

**3.2.1 Synthesis of methyl benzoate (2).** Benzoic acid (24.4398 g, 200 mmol) was dissolved in methanol (80 mL) in a 500 mL round-bottom flask. Concentrated H$_2$SO$_4$ (95%, 7.60 g) was added dropwise under vigorous stirring. The mixture was refluxed at 120 °C for 6 h, with progress monitored hourly *via* TLC. Upon completion, excess methanol was removed by distillation. The cooled residue was transferred to a separatory funnel; the organic layer was isolated, and the aqueous phase was extracted with *n*-hexane (3 × 20 mL). The combined organic fractions were washed with saturated Na$_2$CO$_3$ (2 × 10 mL) and deionized water (2 × 10 mL), then dried over anhydrous Na$_2$SO$_4$. After solvent evaporation, the crude product was purified by fractional distillation, collecting the portion boiling at 195–198 °C. The product identity was confirmed by $^1$H-NMR and melting point analysis.

The colorless, clear, oily liquid with a strong minty odor was obtained with 49% (13.4118 g). $R_f$ = 0.78 (*n*-Hexane : ethyl acetate = 4 : 1, *v/v*). B.p. = 195–198 °C. $^1$H NMR (500 MHz, CDCl$_3$): $\delta$ = 8.04 (d, $J$ = 7.5 Hz, 2H), 7.56 (t, $J$ = 7.5 Hz, 1H), 7.44 (t, $J$ = 7.5 Hz, 2H), 3.92 (s, 3H) ppm.

**3.2.2 Synthesis of benzohydrazide (3).** Hydrazine was first liberated by reacting hydrazine sulfate (26.0000 g, 200 mmol) with potassium hydroxide (22.4440 g, 400 mmol) in a sealed round-bottom flask. The mixture was agitated vigorously, with intermittent cooling in a water bath to manage the exothermic nature of the process. Following stabilization at room temperature, ethanol (100 mL) was added to facilitate the precipitation of the intermediate.

Subsequently, methyl benzoate (13.0870 g, 96.2 mmol) was introduced to the mixture. The reaction was maintained at reflux (130 °C, sand bath) for 8 h, with progress monitored by TLC. The resulting solid was isolated *via* filtration, washed with

**Table 3** Comparison with several other synthetic methods for 2,5-disubstituted-1,3,4-oxadiazole frameworks

| Entry | Substrates | Catalyst | Conditions | Yield (%) | Ref. |
|---|---|---|---|---|---|
| 1 | (*t*-Butoxycarbonyl)phenylalanine | SOCl$_2$, pyridine | Multi-step | 30 | 55 |
| 2 | 1-(2-Bromo-2-nitroethyl)-4-methoxybenzene, ethyl hydrazinecarboxylate | KI (2 eq.), UHP (1 eq.), K$_2$CO$_3$ (2 eq.) | 0 °C, 20 h, DME-H$_2$O | 70 | 56 |
| 3 | Benzohydrazide, 4-methoxylbenzaldehyde | Ceric ammonium nitrate | Reflux, CH$_2$Cl$_2$, 11 h | 67 | 57 |
| 4 | Hydrazide, phenylglyoxylic acid | Eosin Y | Hν, DMF, 45 °C, 12 h | 78 | 58 |
| 5 | (4-Fluorobenzylidene)benzohydrazide | CuI/Bent-NH$_2$ (40 mg), K$_2$CO$_3$ (3 eq.), K$_2$S$_2$O$_8$ (2 eq.) | 100 °C, 5 h, DMSO (1 mL) | 67 | This work |

ethanol ($2 \times 20$ mL), and the filtration was concentrated by slow evaporation to yield additional needle-like crystals. The combined crude product was collected using a fritted glass funnel, washed with cold deionized water until the amber impurities were removed, and dried in a desiccator. The identity and purity of the benzohydrazide product were confirmed by $^1$H-NMR and melting point analysis.

The white solid was obtained with 76% (9.9722 g). $R_f = 0.25$ (ethyl acetate = 100%, $v/v$). M.p. = 114–116 °C [Lit.: 113–115 °C].60 $^1$H NMR (500 MHz, Methanol-$d_4$): $\delta$ = 7.79–7.77 (m, 2H), 7.53 (t, $J$ = 7.5 Hz, 1H), 7.45 (t, $J$ = 7.5 Hz, 2H) ppm.

**3.2.3 Synthesis of ($E$)-$N'$-benzylidenebenzohydrazide (5a).** Benzohydrazide (2.7465 g, 20 mmol) was suspended in ethanol (50 mL) in a round-bottom flask. Benzaldehyde (2.3604 g, 22.2 mmol) was added, and the mixture was stirred until a clear solution was obtained. The reaction was maintained at reflux (120 °C) for 3 h. Subsequently, the solvent was partially evaporated to induce crystallization. The resulting crystalline product was collected *via* a fritted glass funnel, washed with cold methanol, and air-dried. Final traces of moisture were removed in a desiccator. The identity and purity of the product were confirmed by $^1$H-NMR spectroscopy and melting point analysis.

The white solid was obtained with 96% (3.9122 g). $R_f = 0.6$ (*n*-Hexane : ethyl acetate = 4 : 6, $v/v$). M.p. = 214 °C. $^1$H NMR (500 MHz, DMSO-$d_6$): $\delta$ = 11.86 (s, 1H), 8.47 (s, 1H), 7.93 (d, $J$ = 7.5 Hz, 2H), 7.74 (d, $J$ = 6.5 Hz, 2H), 7.60 (t, $J$ = 7.0 Hz, 1H), 7.53 (t, $J$ = 7.0 Hz, 2H), 7.48–7.44 (m, 3H) ppm.

**3.2.4 Synthesis of 2,5-disubstituted-1,3,4-oxadiazoles.** A glass vial was charged with hydrazone (0.1121 g, 0.5 mmol), $K_2S_2O_8$ (0.2703 g, 1.0 mmol), $K_2CO_3$ (0.2073 g, 1.5 mmol), and the catalyst (20 mg, 40 mg mmol$^{-1}$ relative to hydrazone) in anhydrous DMSO (1 mL). The mixture was stirred at 100 °C for 5 h. After completion, the reaction was quenched with deionized water (5 mL) under stirring. The resulting suspension was centrifuged, and the aqueous phase was extracted with ethyl acetate ($2 \times 5$ mL). The combined organic layers were washed with water ($2 \times 5$ mL), dried over anhydrous $Na_2SO_4$, and concentrated under reduced pressure. The crude residue was purified by flash column chromatography. Product identity and purity were established *via* $^1$H-NMR, $^{13}$C-NMR spectroscopy, and melting point analysis.

## 4 Conclusions

In summary, this study establishes a green and sustainable protocol for accessing 2,5-disubstituted-1,3,4-oxadiazole derivatives *via* the development of a novel CuI/Bent-NH$_2$ heterogeneous catalyst. By grafting APTES onto the bentonite surface followed by the immobilization of CuI, we engineered a material characterized by its distinct layered architecture and superior thermal stability. The catalytic utility of CuI/Bent-NH$_2$ was demonstrated in the synthesis of oxadiazoles, where it efficiently mediated the intramolecular cyclization of ($E$)-$N'$-benzylidenebenzohydrazide precursors. A key innovation of this methodology is the synergistic combination of the heterogeneous catalyst with $K_2S_2O_8$ – an environmentally benign oxidant – facilitating a clean cyclization process. Notably, the catalyst's

exceptional durability and ease of recovery *via* simple filtration demonstrate a significant leap toward sustainable industrial applications. This work highlights the transformative potential of functionalized clay minerals, positioning them as cost-effective alternatives to homogeneous catalysts in modern green organic synthesis.

## Author contributions

Vinh Quang Tran: investigation, methodology, resources, formal analysis, validation, data curation, and writing – original draft. Dat Minh Tran: resources, validation, data curation, writing – original draft. Minh Hai Tran: resources, validation, data curation, writing – original draft. Phuong Hoang Tran: methodology, resources, writing – review and editing. Hai Truong Nguyen: methodology, resources, formal analysis, validation, data curation, writing – review and editing, and supervision.

## Conflicts of interest

The authors declare that they have no known competing financial interests or personal relationships that could have appeared to influence the work reported in this paper.

## Data availability

Data will be made available on request.

Supplementary information is available. See DOI: https://doi.org/10.1039/d5ra09105e.

## Acknowledgements

## References

1 A. Weyesa and E. Mulugeta, *RSC Adv.*, 2020, **10**, 20784–20793.
2 E. Zarenezhad, M. Farjam and A. Iraji, *J. Mol. Struct.*, 2021, **1230**, 129833.
3 J. Farhat, L. Alzyoud, M. Alwahsh and B. Al-Omari, *Cancers*, 2022, **14**, 2196.
4 A. Singh, G. Singh and P. M. S. Bedi, *J. Heterocyclic Chem.*, 2020, **57**, 2658–2703.
5 A. Singh, D. Malhotra, K. Singh, R. Chadha and P. M. S. Bedi, *J. Mol. Struct.*, 2022, **1266**, 133479.
6 G. B. Poonam, R. Srivastava and R. Singh, *J. Iran. Chem. Soc.*, 2022, **19**, 665–677.
7 M. Luczynski and A. Kudelko, *Appl. Sci.*, 2022, **12**, 3756.
8 A. Ilangovan, S. Saravanakumar and S. Umesh, *J. Chem. Sci.*, 2015, **127**, 797–801.
9 S. Nayak, S. L. Gaonkar, E. A. Musad and A. M. A. L. Dawsar, *J. Saudi Chem. Soc.*, 2021, **25**, 101284.
10 S. Wacławek, V. V. T. Padil and M. Černík, *Ecol. Chem. Eng. S*, 2018, **25**, 9–34.

11 K. Sanavada, M. Shah, D. Gandhi, A. Unnarkat and P. Vaghasiya, *Environ. Nanotechnol. Monit. Manag.*, 2023, **20**, 100784.

12 S. Jeenpadiphat and D. N. Tungasmita, *Appl. Clay Sci.*, 2014, **87**, 272–277.

13 N. Nouri, M. Tasviri and S. Zendehboudi, *Ind. Eng. Chem. Res.*, 2023, **62**, 6612–6625.

14 Y. S. Kurniawan, A. C. Imawan, Y. M. Stansyah and T. D. Wahyuningsih, *J. Environ. Chem. Eng.*, 2021, **9**, 105508.

15 I. W. Khan, A. Naeem, M. Farooq, T. Mahmood, B. Ahmad, M. Hamayun, Z. Ahmad and T. Saeed, *Renewable Energy*, 2020, **155**, 181–188.

16 B. Eftekhari far and M. Nasr-Esfahani, *Appl. Organometal. Chem.*, 2020, **34**, e5406.

17 S. Sadjadi and F. Koohestani, *J. Mol. Liq.*, 2020, **319**, 114393.

18 M. Nasrollahzadeh, T. Baran, M. Sajjadi, N. Yılmaz Baran and M. Shokouhimehr, *J. Mater. Sci.: Mater. Electron.*, 2020, **31**, 12856–12871.

19 B. Krishnan and S. Mahalingam, *J. Mol. Liq.*, 2017, **241**, 1044–1058.

20 R. Vinodh, Y. Sasikumar, M. Palanichamy, R. Atchudan and T. Ahamad, *Mater. Lett.*, 2021, **294**, 129811.

21 N. Bahri-Laleh and S. Sadjadi, *Res. Chem. Intermed.*, 2018, **44**, 6351–6368.

22 L. S. Kostenko, I. I. Tomashchuk, T. V. Kovalchuk and O. A. Zaporozhets, *Appl. Clay Sci.*, 2019, **172**, 49–56.

23 I. Abad, J. Jiménez-Millán, J. M. Molina, F. Nieto and J. A. Vera, *Clays Clay Miner.*, 2003, **51**, 543–554.

24 C. Aguzzi, P. Cerezo, C. Viseras and C. Caramella, *Appl. Clay Sci.*, 2007, **36**, 22–36.

25 P. V. Chavan, S. P. Charate, U. V. Desai, C. V. Rode and P. P. Wadgaonkar, *ChemistrySelect*, 2019, **4**, 7144–7150.

26 V. Krupskaya, L. Novikova, E. Tyupina, P. Belousov, O. Dorzhieva, S. Zakusin, K. Kim, F. Roessner, E. Badetti, A. Brunelli and L. Belchinskaya, *Appl. Clay Sci.*, 2019, **172**, 1–10.

27 Y. Uozumi, T. Sato and A. Ohno, *Synfacts*, 2015, **11**, 1330.

28 J. Amaya, L. Bobadilla, L. Azancot, M. Centeno, S. Moreno and R. Molina, *Mater. Res. Bull.*, 2020, **123**, 110728.

29 J. Luo, Y. Luo, J. Yao, M. Zhang, S. Chen and X. Liu, *Appl. Clay Sci.*, 2019, **168**, 450–458.

30 J. Madejová, *Vib. Spectrosc.*, 2003, **31**, 1–10.

31 L. Lisuzzo, G. Cavallaro, S. Milioto and G. Lazzara, *Appl. Clay Sci.*, 2020, **185**, 105416.

32 S. Boonyuen, S. M. Smith, A. Luengnaruemitchai, P. N. Nakorn, Y. Tangjaideborisu and P. Shanmugam, *Inorg. Chem. Commun.*, 2025, **173**, 113862.

33 H. Raclavska, D. Juchelkova, V. Roubicek and D. Matysek, *Fuel Process. Technol.*, 2011, **92**, 13–20.

34 M. F. Brigatti, E. Galan and B. K. G. Theng, in *Developments in Clay Science*, ed F. Bergaya, B. K. G. Theng and G. Lagaly, Elsevier, 2006, vol. 1, pp. 19–86.

35 B. C. Erdoğan and S. Ülkü, *Appl. Clay Sci.*, 2011, **54**, 217–225.

36 S. Carquigny, J. Takadoum and S. Ivanescu, *Eur. Phys. J. Appl. Phys.*, 2019, **85**, 21301.

37 G. G. Lara, G. F. Andrade, M. F. Cipreste, W. M. da Silva, P. L. Gastelois, D. A. Gomes, M. C. de Miranda, W. A. de Almeida Macedo, M. J. Neves and E. M. B. de Sousa, *J. Mater. Sci.: Mater. Med.*, 2018, **29**, 130.

38 X. Chen, X. Wang and D. Fang, *Fuller. Nanotub. Car.N.*, 2020, **28**, 1048–1058.

39 P. V. F. de Sousa, A. F. de Oliveira, A. A. da Silva and R. P. Lopes, *Environ. Sci. Pollut. Res.*, 2019, **26**, 14883–14903.

40 N. Ghazal, M. Madkour, A. Abdel Nazeer, S. S. A. Obayya and S. A. Mohamed, *RSC Adv.*, 2021, **11**, 39262–39269.

41 V. Umrigar, M. Chakraborty and P. Parikh, *J. Inst. Eng. India Ser. E*, 2020, **101**, 109–114.

42 S. Zazouli, L. Lâallam and E. M. Ketatni, *J. Mol. Struct.*, 2021, **1239**, 130465.

43 H. Ullah, I. Uddin, Misbah, F. Khan, M. Taha, F. Rahim, M. Sarfraz, S. Shams, M. Nabi and A. Wadood, *Chem. Data Coll.*, 2021, **36**, 100778.

44 S. Syed Tajudeen and G. Kannappan, *J. Pharm. Res.*, 2013, **7**, 534–539.

45 S. Mandal, T. Bera, G. Dubey, J. Saha and J. K. Laha, *ACS Catal.*, 2018, **8**, 5085–5144.

46 M. C. Leech and K. Lam, *Nat. Rev. Chem.*, 2022, **6**, 275–286.

47 C. Kingston, M. D. Palkowitz, Y. Takahira, J. C. Vantourout, B. K. Peters, Y. Kawamata and P. S. Baran, *Acc. Chem. Res.*, 2020, **53**, 72–83.

48 S. Guin, T. Ghosh, S. K. Rout, A. Banerjee and B. K. Patel, *Org. Lett.*, 2011, **13**, 5976–5979.

49 B. Zhu, H. Cheng, Y. Qin, J. Ma, Y. Kong and S. Komarneni, *Sep. Purif. Technol.*, 2020, **233**, 116057.

50 Q. Wu, C. Yang, X. Man, X. Li, Q. Wu, Y. Zhang, D. Jiang and Z. Qi, *Tetrahedron*, 2026, **190**, 135036.

51 R. A. Rather, S. Siddiqui, W. A. Khan and Z. N. Siddiqui, *Mol. Catal.*, 2020, **490**, 110975.

52 S. Soni, P. Teli, N. Sahiba, S. Teli and S. Agarwal, *RSC Adv.*, 2023, **13**, 13337–13353.

53 R. A. Sheldon, *ACS Sustain. Chem. Eng.*, 2018, **6**, 32–48.

54 E. A. Elkhatib, M. L. Moharem, A. F. Saad and F. A. Attia, *Sci. Rep.*, 2022, **12**, 8412.

55 S. Borg, G. Estenne-Bouhtou, K. Luthman, I. Csoeregh, W. Hesselink and U. Hacksell, *J. Org. Chem.*, 1995, **60**, 3112–3120.

56 K. Tokumaru and J. N. Johnston, *Chem. Sci.*, 2017, **8**, 3187–3191.

57 M. Dabiri, P. Salehi, M. Baghbanzadeh and M. Bahramnejad, *Tetrahedron Lett.*, 2006, **47**, 6983–6986.

58 P. Diao, Y. Ge, W. zhang, C. Xu, N. Zhang and C. Guo, *Tetrahedron Lett.*, 2018, **59**, 767–770.

59 N. Myeni, S. K. Ghosh, V. K. Perla and K. Mallick, *Mater. Res. Express*, 2019, **6**, 1050a1057.

60 J. N. Asegbeloyin, O. T. Ujam, E. C. Okafor, I. Babahan, E. P. Coban, A. Özmen and H. Biyik, *Bioinorg. Chem. Appl.*, 2014, **2014**, 718175.